ChemComm

ROYAL SOCIETY OF CHEMISTRY

FEATURE ARTICLE

View Article Online
View Journal

Cite this: DOI: 10.1039/d6cc01787h

Hydridoborate solid electrolytes: opportunities and challenges

Hugo Braun, [ab] Corsin Battaglia [acd] and Arndt Remhof *[ab]

Hydridoborates have emerged as a distinct class of inorganic solid electrolytes with exceptional potential for solid-state batteries. Their lithium and sodium salts with polyhedral *closo*- and *closo*-carba-hydridoborate anions offer low crystallographic density, mechanical softness suitable for cold pressing, and broad electrochemical stability, enabling integration with alkali metal anodes and high-voltage cathodes. Superionic transport arises from order–disorder transitions and the resulting rotational dynamics of the cage anions, which create a highly connected and dynamically accessible network of Li^+ and Na^+ migration pathways. So far, electrolyte synthesis is costly, due to the close chemical relationship among boron–hydrogen clusters that leads to low selectivity and often produces mixtures of hydridoborates that are difficult to separate. Most reported routes are multistep procedures involving elevated temperatures, extended reaction times, solvent handling, and purification steps. Synthetic routes based on inexpensive $NaBH_4$ precursors, and direct synthesis of mixed-anion electrolytes instead of pure hydridoborate salts showcase promising paths toward scalable cost-effective synthesis. Finally, recently discovered mechanisms of hydridoborate oxidation and reduction are outlined, and their integration into solid-state batteries is summarized. By linking structural chemistry, transport mechanisms, and device-level behavior, this Feature Article outlines key design principles and future directions for hydridoborate solid electrolytes in next-generation solid-state batteries.

Received 24th March 2026,
Accepted 8th May 2026

DOI: 10.1039/d6cc01787h

rsc.li/chemcomm

[a] *Empa – Swiss Federal Laboratories for Materials Science and Technology, Dübendorf, Switzerland. E-mail: arndt.remhof@empa.ch*
[b] *Institut für Anorganische und Analytische Chemie, Universität Freiburg, Germany*
[c] *Department of Information Technology and Electrical Engineering, ETH Zurich, Zürich, Switzerland*
[d] *Institute of Materials, School of Engineering, EPFL, Lausanne, Switzerland*

Hugo Braun

Hugo Braun is a PhD student in Chemistry at the University of Freiburg, conducting his research in Empa's laboratory Materials for Energy Conversion under the supervision of PD Dr Arndt Remhof and Prof. Dr Ingo Krossing. His work focuses on the development and electrochemical characterization of hydridoborate-based solid-state batteries. He holds an MSc and BSc in Mechanical Engineering from ETH Zurich, with research experience in solid-state electrolytes, solar-driven CO_2 splitting, and chemoresistive gas sensors. He has industrial experience at Northvolt and Sensirion and contributes to teaching battery materials and characterization at ETH Zurich.

Corsin Battaglia

Corsin Battaglia directs Empa's laboratory Materials for Energy Conversion and is Adjunct Professor at ETH Zurich and EPFL. He received his PhD from the Université de Neuchâtel and held postdoctoral positions at EPFL, the University of California, Berkeley, and Lawrence Berkeley National Laboratory before joining Empa in 2014.

1. Introduction and background

Solid-state batteries are widely regarded as promising alternative to today's lithium-ion battery technology, offering improved safety, higher specific energy and energy density, and the possibility of using alkali metal anodes.[1] Central to their performance is the solid electrolyte, which must combine high ionic conductivity at ambient temperature with wide electrochemical stability, mechanical compliance, and scalable cost-effective synthesis. Despite intense research activity, no single class of solid electrolytes has yet fulfilled all these requirements simultaneously.[2]

Polymers, oxides, sulfides, and halides have each demonstrated notable strengths, but also intrinsic limitations. Polymer electrolytes are mechanically flexible yet suffer from low room-temperature conductivity.[3–5] Oxides offer excellent chemical stability but are mechanically rigid and difficult to integrate into composite electrodes. Sulfides provide high ionic conductivity and favorable mechanics but are chemically and electrochemically unstable, particularly toward alkali metal anodes.[6,7] Halide electrolytes have recently attracted attention for high-voltage applications, but their incompatibility with alkali metal necessitates protective interlayers.[8] These trade-offs continue to motivate the search for alternative solid electrolyte chemistries.[2,9] Mechanical properties are increasingly recognized as a key differentiator among these classes: soft and compliant electrolytes can better conform to active materials, maintain intimate interfacial contact, and mitigate the formation of localized stress and current hotspots that promote dendrite growth.[10,11]

In this context, hydridoborates (aka hydroborates), inorganic salts featuring boron and hydrogen based polyanions, have emerged as a distinct and highly promising class of solid electrolytes.[12] A key turning point was the discovery by Orimo *et al.* that $LiBH_4$ undergoes a transition to a superionic phase above 110 °C, exhibiting ionic conductivities exceeding 10^{-3} S cm^{-1}, which established complex hydrides as viable fast-ion conductors.[13] Subsequent studies showed that strategies such as anion substitution,[14–16] nanoconfinement,[17,18] and nanosizing by mechano-chemical milling[19–21] can stabilize highly conductive phases down to room temperature. However, the limited electrochemical stability of simple borohydrides motivated a shift toward more complex anions, in particular *closo*-hydridoborates ($M(B_nH_n)$, M = Li, Na) and *closo*-carba-hydridoborates ($M(CB_{n-1}H_n)$, M = Li, Na) featuring rigid polyhedral frameworks and delocalized charge. Their ion transport relies on anion-assisted hopping mechanisms enabled by orientational disorder of the cage anions, giving rise to high ionic conductivity when structural disorder is appropriately engineered.[22,23]

Representative ionic conductivities of disordered mixed-anion hydridoborates illustrate the effectiveness of disorder engineering. A single-phase equimolar mixture of $Li_2B_{10}H_{10}$ and $Li_2B_{12}H_{12}$ exhibits conductivities of 4×10^{-4} S cm^{-1} at 25 °C and 4×10^{-3} S cm^{-1} at 60 °C, several orders of magnitude higher than either parent compound.[21] Even higher room-temperature conductivities, ranging from 6.9×10^{-5} to 6.7×10^{-3} S cm^{-1}, have been reported for mixed *closo*-monocarba-hydridoborates $(1-x)LiCB_9H_{10}$–$xLiCB_{11}H_{12}$ (x = 0.1–0.9).[24–26] Sodium analogues generally conduct even faster, with $Na_2(CB_{11}H_{12})(CB_9H_{10})$ reaching 7×10^{-2} S cm^{-1} at 27 °C,[27] placing it among the highest-conductivity solid electrolytes reported to date. These values underscore that hydridoborates can achieve liquid-like ionic conductivities while retaining wide electrochemical stability and favorable mechanical properties.

In the technologically relevant temperature window from −40 °C to 120 °C, hydridoborate electrolytes do not follow a single Arrhenius-type transport mechanism. Their apparent activation energies increase toward lower temperatures, with values around ∼0.7 eV commonly observed in the sub-ambient regime, while at elevated temperatures activation energies decrease to ∼0.2–0.4 eV.[28,29] This reflects a transition from correlated ion motion, dominated by strong ion–ion interactions and collective hopping constraints at low temperature, to uncorrelated, thermally activated transport once these interactions are sufficiently overcome.[28]

Importantly, recent cell-level demonstrations confirm that this transport mechanism remains sufficiently active even at sub-zero temperatures. A sodium hydridoborate solid-state battery was shown to operate at −10 °C, delivering an areal capacity of 2.5 mAh cm^{-2} with a $NaCrO_2$ cathode and Sn anode, demonstrating that low-temperature operation is feasible despite the increased activation barriers in this regime.[30]

These values underscore that hydridoborates can achieve liquid-like ionic conductivities while retaining wide electrochemical stability and favorable mechanical properties.

A defining feature of these electrolytes is the ability to tune this disorder, most effectively through compositional anion mixing, which stabilizes highly conductive phases down to room temperature. Due to their wide electrochemical stability window, and their slow reduction and/or oxidation kinetics outside of the electrochemical stability window, integration with alkali metal anodes and high-voltage cathodes has been demonstrated.[15,25,29,31,32] As a result, hydridoborates have progressed from model fast-ion conductors to functional

Arndt Remhof

Arndt Remhof is a group leader at Empa's laboratory Materials for Energy Conversion and holds a teaching assignment at Albert-Ludwigs-Universität Freiburg, where he habilitated in 2019. His research focuses on next-generation lithium- and sodium-ion batteries and solid-state battery materials. He studied physics at Ruhr-University Bochum and University of Kent, received his PhD in Bochum, and worked as a postdoc at Free University of Amsterdam. He joined Empa in 2007 and completed a sabbatical at Humboldt-Universität zu Berlin in 2023.

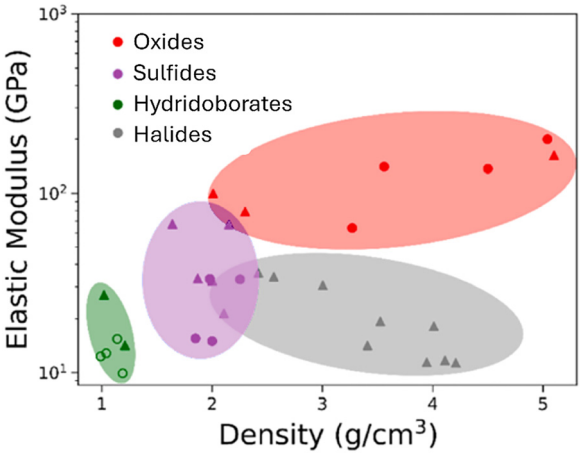

Fig. 1 Ashby plot of elastic modulus and density for different types of solid electrolytes. Circle data points are from experimentally reported values while triangles are from first-principles calculations. Adapted from ref. 33 with permission from Elsevier,[33] copyright 2025.

electrolytes in full solid-state battery cells. Provided that scalable, cost-effective synthesis routes are developed in the future, hydridoborates are attractive for large-scale application in solid-state batteries, given their low crystallographic density, soft mechanical properties enabling cold pressing, good thermal stability, low toxicity, and solution-processability.[12] Recent nanoindentation studies show that the average elastic moduli of *closo*-carba-hydridoborate salts fall within a narrow range (≈11.2–12.3 GPa), comparable to sulfides and halides, with $NaCB_{11}H_{12}$ exhibiting an even lower modulus of ≈8.8 GPa.[33] This mechanical softness, combined with low density, positions hydridoborates in a favorable region of the modulus–density design space, as illustrated in Fig. 1.

In this Feature Article, we review the chemistry, structure, and electrochemical properties of *closo*- and *closo*-carba-hydridoborate solid electrolytes for lithium- and sodium-based solid-state batteries. Hydridoborates uniquely combine several attributes that directly address the limitations of mainstream solid electrolytes: they offer mechanical softness enabling cold pressing, thermal and chemical robustness, high ionic conductivity arising from anion-assisted transport, and a wide electrochemical stability compatible with high-voltage cathodes and alkali-metal anodes. This unusual convergence of properties, together with their low crystallographic density, low toxicity, and the prospect of scalable synthesis from inexpensive precursors, positions hydridoborates as a compelling alternative electrolyte chemistry. We discuss structural chemistry, synthesis strategies, ion conduction mechanisms, and electrochemical stability, and examine how these materials can be integrated into practical solid-state battery architectures. By linking fundamental materials chemistry with device-level performance, we aim to identify key design principles and outline future directions for hydridoborate-based solid electrolytes.

2. Chemistry and synthesis of *closo*- and carba-hydridoborate electrolytes

2.1. Structural chemistry of *closo*- and carba-hydridoborate anions

Hydridoborate solid electrolytes relevant for lithium- and sodium-based solid-state batteries are predominantly based on *closo*-hydridoborate anions with ten or twelve vertices, namely $[B_{10}H_{10}]^{2-}$ and $[B_{12}H_{12}]^{2-}$, and their carbon-substituted analogues, the *closo*-carba-hydridoborate anions such as $[CB_9H_{10}]^-$ and $[CB_{11}H_{12}]^-$, shown in Fig. 2. The predominance of these specific cage sizes originates from their exceptional intrinsic stability: as electron-deficient boron clusters, they follow the Wade–Mingos rules, which predict that *closo*-polyhedra with n vertices are most stable when containing $(n + 1)$ skeletal electron pairs. Each BH contains four electrons, of which two form the exoskeletal B–H bond. The remaining two electrons contribute to the polyhedral framework as skeletal electrons, and together with the two additional electrons from the dianionic charge they provide exactly the $(n + 1)$ skeletal electron pairs required for a *closo*-cluster with n vertices. The $[B_{10}H_{10}]^{2-}$ and $[B_{12}H_{12}]^{2-}$ anions satisfy this requirement ideally, giving rise to electronically saturated, highly symmetric polyhedral frameworks with delocalized multicenter bonding. This electronic stabilization, makes 10- and 12-vertex *closo*-clusters significantly more robust than smaller or more open borane species, and therefore they are the natural structural motifs for hydridoborate electrolytes.[34]

These anions adopt rigid, highly symmetric cage structures with delocalized multicenter bonding, resulting in weak electrostatic interactions with mobile alkali cations Li^+ and Na^+.[22,35]

The quasi-spherical charge distribution of these clusters produces a shallow potential energy landscape for Li^+ and

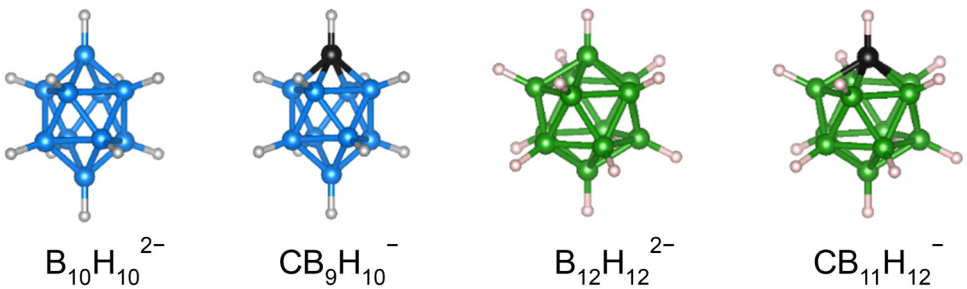

Fig. 2 Examples of *closo*-hydridoborate and *closo*-carba-hydridoborate anions.

Na^+ migration, fundamentally distinguishing hydridoborates from oxide, sulfide, or halide electrolytes with strongly directional bonding. In the solid state, these cage anions frequently exhibit orientational disorder and dynamic reorientation, which contributes entropically to ionic transport.[23] The coupling between anion rotational dynamics and cation hopping establishes a direct link between structural disorder and fast ion conduction, forming the mechanistic basis for the high ionic conductivities discussed in Section 3.

Among the available cage sizes, twelve-vertex systems play a particularly prominent role due to their exceptional chemical and thermal stability, high symmetry, and favorable solid-state dynamics. Consequently, $[B_{12}H_{12}]^{2-}$ and $[CB_{11}H_{12}]^-$-based compounds dominate current hydridoborate electrolyte research, while ten-vertex systems are often employed in mixed-anion compositions to introduce compositional disorder and stabilize superionic phases at room temperature.[29,36]

2.2. General considerations in the synthesis of metal hydridoborates

Metal close-cage *closo*-hydridoborate salts are typically formed through B–H condensation and B–B bond formation processes that require elevated temperatures ($\approx$180 °C or higher). At lower temperatures, less condensed species such as clusters with only few B–B bonds as $[B_3H_8]^-$ or open-cage *nido*- and arachno-clusters are favored, reflecting the hierarchical stability of boron–hydrogen clusters. This temperature dependence governs both deliberate synthesis routes and the formation of hydridoborates as intermediates during the thermal decomposition of metal borohydrides.[35] A close chemical relationship therefore exists between metal borohydrides and higher hydridoborates, as exemplified by the formation of $Li_2B_{12}H_{12}$ during $LiBH_4$ decomposition.[37] This relationship underpins many modern synthesis strategies and enables the use of borohydrides as convenient and inexpensive precursors.

From an application perspective, the current cost structure of hydridoborate salts is influenced less by the price of precursors such as $NaBH_4$ but more by the immaturity of existing synthesis routes. Many reported procedures were originally developed for fundamental cluster chemistry and involve multistep reactions, elevated temperatures, and purification stages that have not yet been optimized for scale. The close chemical relationship among boron–hydrogen clusters can lead to mixtures of products. This challenge increasingly motivates the design of selective and integrated synthesis protocols. Recent advances including mechanochemical processing, solvent-free metathesis, and solution-based mixed-anion syntheses clearly demonstrate pathways toward simpler, safer, and more scalable production. As research attention grows, substantial improvements in process efficiency and cost are expected.

Safety considerations are important throughout hydridoborate synthesis, as certain borane intermediates are toxic, volatile, and air-sensitive. However, many modern routes deliberately avoid the most hazardous lower boranes such as diborane (B_2H_6), favoring solid-state or solution-based transformations starting from stable borohydride precursors.

2.3. Synthetic routes to *closo*-$[B_nH_n]^{2-}$ salts

Several synthetic strategies have been established for the preparation of *closo*-dodecahydridoborate salts, *i.e.* salts with a $[B_{12}H_{12}]^{2-}$ anion. Early approaches relied on the reaction of toxic and explosive B_2H_6 solution with metal borohydrides, yielding boron-rich clusters in which higher temperatures favor the formation of the thermodynamically most stable $[B_{12}H_{12}]^{2-}$ anions.[38] A more recent approach includes solvent-free solid–gas reactions and mechanically assisted methods, such as ball milling, which enhance diborane diffusion through passivating product layers and improve overall yields.[39]

A widely used and comparatively safe approach involves iodine-mediated condensation reactions. In this approach, $NaBH_4$ reacts with iodine in diglyme to form NaB_3H_8, according to $3NaBH_4 + I_2 \rightarrow 2NaI + 2H_2 + NaB_3H_8$ which subsequently undergoes thermal condensation under reflux to yield $Na_2B_{12}H_{12}$. This route avoids the highly toxic diborane precursor and offers a cost-effective pathway, typically followed by acid treatment and cation exchange.[40] Iodine acts as an oxidation agent, accepting electrons as three $[BH_4]^-$ units are partially dehydrogenated and condensed into the nido-cluster $[B_3H_8]^-$, transferring two electrons to the iodine. The formation of $[B_3H_8]^-$ reflects its status as the most stable low-condensed *nido*-cluster accessible. I_2 facilitates this step by oxidizing $[BH_4]^-$ and breaking of B–H bonds while the release of H_2 and the formation of new B–B bonds provide the thermodynamic driving force. Subsequent thermal condensation of $B_3H_8^-$ to *closo*-$[B_{12}H_{12}]^{2-}$ proceeds because the 12-vertex *closo*-cluster represents the thermodynamic endpoint of boron–hydrogen cluster growth, stabilized by extensive delocalized multicenter bonding.[41]

Decaborane ($B_{10}H_{14}$) has also served as a versatile precursor for the synthesis of $[B_{12}H_{12}]^{2-}$ and $[B_{10}H_{10}]^{2-}$ anions, despite its toxicity and volatility.[42] Both solution-based and solvent-free solid-state reactions with metal borohydrides at temperatures between 200 and 450 °C have been demonstrated, enabling direct access to alkali and alkaline-earth metal dodecahydridoborates.[43]

Ion-exchange and metathesis reactions provide additional synthetic flexibility. Alkali metal dodecahydridoborates can be converted into *closo*-dodecaboric acid using strongly acidic ion-exchange resins, followed by reaction with metals, oxides, or carbonates to yield the desired metal salts. Products obtained *via* aqueous routes are frequently hydrated and may therefore require additional thermal treatment prior to use.[21,42]

More recently, a scalable, solution-based synthesis has been reported for the direct preparation of the mixed-anion solid electrolyte $Na_4(B_{12}H_{12})(B_{10}H_{10})$ starting from $NaBH_4$. In this multi-step solvothermal process, the *closo*-anions $[B_{10}H_{10}]^{2-}$ and $[B_{12}H_{12}]^{2-}$ are formed *via* a common $[B_3H_8]^-$ intermediate. Their relative formation depends on the balance between reaction temperature, dehydrogenation rate, and the kinetics of B–B bond rearrangement. Under conditions where condensation is incomplete, the 10-vertex *closo*-cluster is kinetically favored, whereas extended reaction times and higher temperatures promote the formation of the thermodynamically more

stable 12-vertex species. The observed 1:1 stoichiometry therefore reflects a controlled interplay of kinetic and thermodynamic factors rather than strict selectivity for a single cluster size.

This strategy illustrates how the inherent chemistry of hydridoborates can be leveraged to synthesize functionally optimized solid electrolytes in a single, solution-based process, offering an attractive pathway toward scalable production.[44]

2.4. Synthetic routes to *closo*-carba-hydridoborates: $CB_{n-1}H_n$ (n = 10, 12)

Closo-carba-hydridoborates are structurally similar to *closo*-hydridoborates, whereby one BH vertex is substituted with a CH unit, yielding monovalent anionic clusters such as $[CB_9H_{12}]^-$ and $[CB_{11}H_{12}]^-$. Among these $[CB_{11}H_{12}]^-$ has emerged as the most relevant *closo*-carba-hydridoborate for solid-state battery electrolytes due to its high symmetry, chemical robustness, and favorable electrochemical properties.

The $[CB_{11}H_{12}]^-$-ion was initially accessed through synthetic routes starting from decaborane $B_{10}H_{14}$[45,46] A key breakthrough was reported by Michl *et al.* in 2001, who demonstrated that $[CB_{11}H_{12}]^-$ can be formed directly *via* cage closure of the *nido*-undecaboranate anion $[B_{11}H_{14}]^-$ using dihalocarbenes CX_2 (X = Cl, Br) as the carbon source.[47] These carbenes were generated *in situ* by deprotonation of chloroform or bromoform with sodium ethanolate. While conceptually elegant, this method suffers from intrinsically low yields due to the short-lived nature of dihalocarbenes and the formation of substituted cluster side products.

Subsequent studies have introduced variations and optimizations aimed at improving yield, selectivity, and scalability, including alternative carbene precursors, modified reaction conditions, and improved control over side reactions. More recent work has increasingly focused on developing synthetic pathways that start from borohydride-derived precursors, proceeding *via* $[B_{11}H_{14}]^-$ intermediates toward $[CB_{11}H_{12}]^-$.[48,49] These efforts highlight ongoing, worldwide activities to establish more practical and scalable routes from $NaBH_4$ or related starting materials to *closo*-carba-hydridoborate electrolytes, reflecting the growing importance of these compounds for solid-state battery applications.

2.5. Assessment of synthesis routes and resource considerations

Although hydridoborate synthesis is still at an early stage and quantitative metrics such as cost, energy demand, or industrial throughput are not yet available, several qualitative trends can be identified. Routes based on diborane or decaborane offer good selectivity but face major safety and scalability limitations due to the toxicity and volatility of these intermediates. Iodine mediated condensation of $NaBH_4$ provides a safer and more cost-effective alternative, relying on inexpensive precursors, though it still involves multistep solvent-based processing. Mechanochemical and solvent free metathesis routes reduce reaction complexity and eliminate solvent handling, offering clear advantages for safety and scalability, but their selectivity and yield optimization remain active research areas. Solution based mixed anion syntheses from $NaBH_4$ enable integrated, single pot processes and avoid isolating individual *closo* anions, yet they require careful control of competing condensation pathways to achieve industrial robustness. Overall, the field is transitioning from traditional cluster chemistry protocols toward simpler, safer, and more scalable routes, but substantial process development is still required before reliable cost or scalability assessments can be made.

From a resource perspective, boron is less abundant in the Earth's crust than lithium, yet global reserves are substantial and boron-based chemicals are already produced at industrial scale for applications in glass, ceramics, agriculture, and specialty chemicals. Boron appears on the EU list of critical raw materials primarily due to the geographical concentration of boron ore deposits and associated supply chain vulnerabilities, rather than intrinsic scarcity. Consequently, boron availability is not expected to impose a fundamental constraint on hydridoborate electrolytes. At present, the main limitations for ''scalable, cost-effective synthesis'' arise from the immaturity of existing synthetic routes rather than from raw material availability, and future advances in process design are likely to play a more decisive role in determining cost and scalability.

3. Ion conductivity and electrochemical properties

3.1. Mechanisms of ionic transport

The structural origin of superionic conductivity in these materials is the high-temperature phase transition during which both cation mobility and anion rotational motion emerge simultaneously. In this transition the alkali metal cations undergo positional disorder (sublattice melting), becoming dynamically distributed over multiple accessible crystallographic sites. At the same time, the hydridoborate anions retain their lattice positions but acquire orientational freedom, leading to rotational disorder of the anion sublattice. This combination of cation positional disorder and anion rotational disorder stabilizes high-symmetry plastic-crystal phases—face-centered cubic (fcc) for $Li_2B_{12}H_{12}$ and body-centered cubic (bcc) for $Na_2B_{12}H_{12}$—commonly referred to as *rotator phases* or *plastic crystals* in the sense of ref. 50. Comprehensive crystallographic data (crystal structures, lattice constants, and space groups) for the major hydridoborate electrolytes have been reported by Černý *et al.*[51]

Owing to their stoichiometry and lattice geometry, these high-temperature phases intrinsically host a large number of vacant interstitial sites, enabling long-range cation diffusion without the need for extrinsic doping. The initial occupation of these sites is governed by geometric considerations consistent with Linus Pauling's first rule, which predicts the preferred cation coordination number from the cation-to-anion radius ratio.[52] In *closo*-hydridoborates and *closo*-carba-hydridoborates, the anions are approximately spherical, and their high symmetry leads to crystal structures that can be viewed as packings of large quasi-spherical anions with cations occupying the

available interstitial voids, fully in line with Pauling's framework for ionic solids.

Based on the estimated anion radius of $r_{(A^-)}$ = 3.28 Å for $B_{12}H_{12}^{2-}$,[53] as a representative of a *closo*-hydridoborate or *closo*-carba hydridoborate anion, the radius ratios $r_{(Li^+)}/r_{(A^-)} \approx 0.18$–$0.23$ (using Li^+ radii $r_{(Li^+)} \approx 0.60$–0.76 Å) fall between the minimum geometric limits for trigonal (0.155) and tetrahedral (0.225) coordination. Consequently, Li^+ tends to occupy low-coordination environments such as trigonal or tetrahedral sites. For Na^+, the corresponding ratio $r_{(Na^+)}/r_{(A^-)} \approx 0.30$ (using Na^+ radii $r_{(Na^+)} \approx 1.0$ Å) lies above the tetrahedral stability threshold yet remains well below the octahedral limit (0.414), indicating a preference for tetrahedral coordination with possible access to higher-coordination environments depending on local geometry. Due to the similar size of $[B_{12}H_{12}]^{2-}$ and $[B_{10}H_{10}]^{2-}$, the geometric considerations can be generalized to mixed-anion hydridoborate salts. Fig. 3 depicts the fcc structure of $Na_4(B_{10}H_{10})(B_{12}H_{12})$. The $[B_{10}H_{10}]^{2-}$ and $[B_{12}H_{12}]^{2-}$ randomly occupy the fcc sites, the rotational disorder is implied by the arrows, Interstitial sites with tetrahedral symmetry are marked in red, and interstitial sites with octahedral symmetry are represented in yellow.

Importantly, the high-symmetry anion packings that form in the plastic-crystal (rotator) phases, typically cubic close-packed (ccp/fcc) or body-centered cubic (bcc), generate a dense array of interconnected interstitial sites. *Ab initio* molecular dynamics simulations show that several of these site types are energetically near-degenerate and dynamically accessible.[22] This near-degeneracy creates a remarkably flat energy landscape with only weak site preference, leading to a structurally frustrated cation sublattice in which no unique equilibrium site is strongly favored. In concert with the rotational dynamics of the anions, this frustrated, highly disordered cation network underpins the emergence of superionic conductivity.

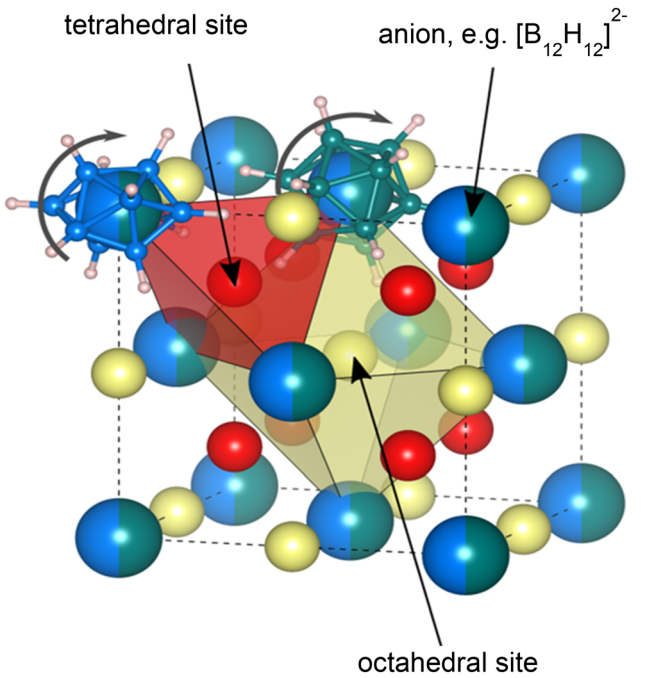

Fig. 3 Crystal structure of $Na_4B_{10}H_{10}B_{12}H_{12}$. The fcc sites are randomly occupied with $[B_{10}H_{10}]^{2-}$ and $[B_{12}H_{12}]^{2-}$ anions. Interstitial sites with tetrahedral symmetry are marked in red, the ones with octahedral symmetry are represented in yellow. Reproduced from ref. 15 with permission from the Royal Society of Chemistry,[15] copyright 2017.

A second, complementary contribution arises from local bond frustration associated with the interaction between mobile cations and the nearly spherical *closo*-hydridoborate anions. Calculations on isolated cation–anion pairs show that when a Li^+ approaches a $[B_{12}H_{12}]^{2-}$ anion, it preferentially binds near the center of a triad of boron atoms, reflecting the intrinsic symmetry of the icosahedral cluster.[22] These preferred docking positions, however, do not generally coincide with the symmetry-imposed sites of the crystal lattice. As a result, cations experience competing energetic preferences imposed by the anion symmetry on the one hand and the lattice symmetry on the other hand, further destabilizing static site occupation and promoting hopping between neighboring positions.

Taken together, the presence of vacant interstitial sites, the high density of energetically accessible sites, and the mismatch between anion and lattice symmetry create a highly frustrated potential lattice that favors the formation of mobile cation excitations and facilitates long-range diffusion.

A third and equally important ingredient is dynamical frustration, arising from the low-frequency lattice vibrations and facile re-orientational motion of the cluster anions. Experimental probes such as neutron scattering, solid-state NMR, and muon-based spectroscopies have shown that anion re-orientational dynamics and cation diffusion occur on comparable time scales and are strongly correlated.[28,54,55] The reorientation of the anions dynamically modulates the local electrostatic environment, leading to temporal fluctuations of migration barriers and effectively providing a local driving force for cation motion. This dynamic disorder in anion orientation not only enhances short-range mobility but also supports long-range, liquid-like diffusion in the superionic state.

The factors leading to a flattened energy landscape and thus promoting ionic conduction are schematically shown in Fig. 4.

The mechanistic concepts outlined above, initially established for alkali-metal *closo*-dodecahydridoborates ($M_2B_{12}H_{12}$), extend naturally to the corresponding *closo*-carba-hydridoborate compounds $MCB_{n-1}H_n$ (n = 10, 12) and mixed-anion compounds. Carba-hydridoborate anions possess a similar size, near-spherical geometry, and rigid polyhedral framework, leading to closely related crystal structures and comparable distributions of interstitial sites. As a result, structural frustration, local bond frustration arising from anion–lattice symmetry mismatch, and dynamical frustration associated with anion reorientations are also present in these materials and give rise to fast alkali-ion transport.

A key difference, however, lies in the lower anion charge of the carba-hydridoborates, which carry a single negative charge instead of two. This lower charge density results in weaker electrostatic attraction between the anions and the mobile

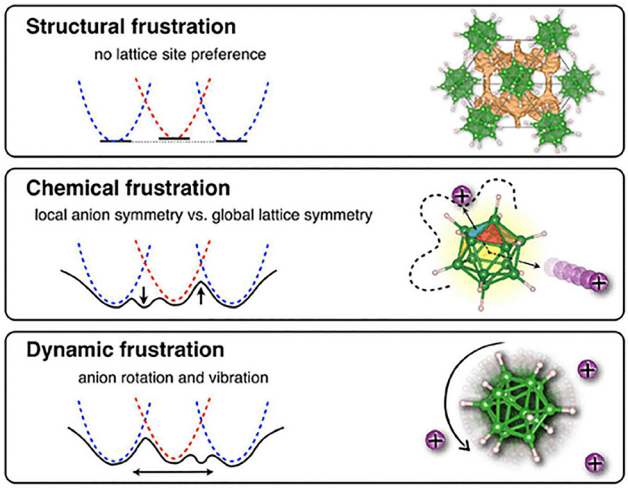

Fig. 4 Effect of structural, chemical, and dynamical frustration on energy landscape. (a) Geometric site frustration removes strong site preferences, creating multiple minima in the energy landscape. (b) Frustration between the local anion geometry and crystal lattice symmetry creates additional local minima. (c) Anion dynamics introduces fluctuations in the perturbing potential. Reproduced from ref. 23 with permission from the American Chemical Society,[23] copyright 2017.

cations, as well as a lower cation concentration in the lattice. Both effects modify the balance between site occupancy and mobility, influencing activation energies and absolute conductivities, while preserving the underlying transport mechanism. These distinctions highlight the tunability of hydridoborate electrolytes through anion chemistry, enabling systematic control over electrostatic interactions and charge-carrier density without fundamentally altering the transport framework.

3.2. Electrochemical stability and compatibility

Beyond their favorable transport properties, *closo-* and *closo*-carba-hydridoborate electrolytes exhibit wide electrochemical stability windows, a key prerequisite for their integration into all-solid-state batteries with high energy and power density and long cycle life. High oxidative stability is particularly important, as it enables the use of high-voltage cathodes and thus directly impacts achievable cell-level specific energy. Determining electrochemical stability windows for solid-state electrolytes, however, is far more challenging than for liquid electrolytes, primarily due to slow decomposition kinetics and the intrinsically low electronic conductivity for solid electrolytes.[56,57]

A common method to determine the oxidative stability is linear sweep voltammetry on a pelletized electrolyte sandwiched between an inert blocking electrode (*e.g.* Pt or stainless steel) and a Li or Na counter electrode, respectively. Fig. 5a illustrates this configuration. The limited interfacial contact between the electrode and the solid electrolyte and the low electronic conductivity of the electrolyte result in small decomposition currents that can easily be missed, especially at high sweep rates.

A widely used strategy to address the challenge of low decomposition currents is the preparation of composite electrodes consisting of the solid electrolyte and conductive carbon additives. These composites establish interpenetrating ionic and electronic conduction pathways and allow electrochemical reactions to proceed at measurable rates as illustrated in Fig. 5b. Fig. 5c shows linear sweep voltammetry of $LiBH_4$ using (i) no carbon, (ii) low-surface-area carbon, and (iii) high-surface-area carbon. Increasing the carbon surface area shifts the onset of decomposition to lower potentials.[58,59] This approach is straightforward for soft, plastically deformable electrolytes such as sulfides and hydridoborates, which readily form intimate contact with carbon upon cold pressing. In contrast, rigid oxide electrolytes often require high-temperature sintering to achieve sufficient ionic and electronic percolation.[60] Owing to their mechanical softness and processability, hydridoborate electrolytes are well suited for such composite-based measurements. Nevertheless, earlier experimental reports on their oxidative stability showed significant discrepancies with first-principles predictions, in some cases suggesting oxidative stability limits exceeding 5 V *versus* Li^+/Li.[61,62]

Subsequent studies employing carefully designed experimental protocols have clarified this issue. Robust determination of the oxidative onset potential requires slow scan rates (on the

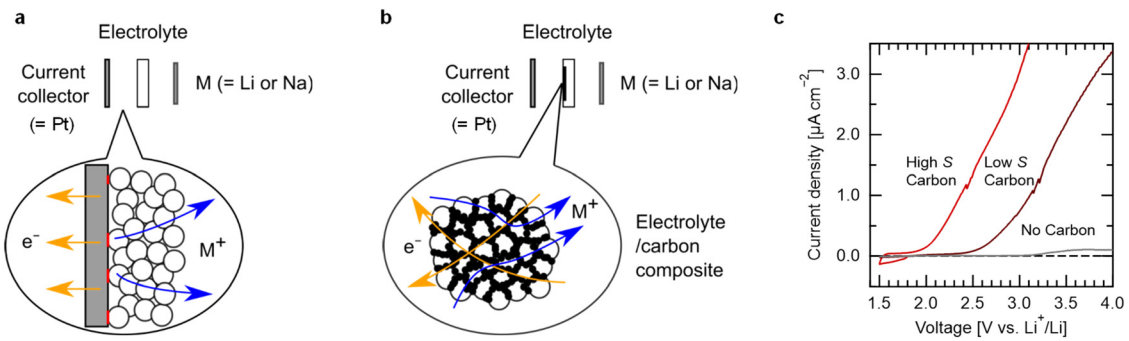

Fig. 5 (a) Schematic of linear sweep voltammetry (LSV) measurement using a pelletized solid electrolyte between an inert blocking electrode and a Li counter electrode. (b) Concept of composite electrodes consisting of solid electrolyte and conductive carbon additives, enabling measurable oxidative decomposition currents. (c) LSV of $LiBH_4$ recorded with (i) no carbon, (ii) low-surface-area carbon, and (iii) high-surface-area carbon, showing the shift of the oxidative onset to lower potentials with increasing carbon surface area. Adapted from ref. 58 with permission from the American Chemical Society,[58] copyright 2019.

order of 10 μV s^{-1}), elevated temperatures of 60 °C to promote interfacial reactions and ionic transport, rigorous separation of capacitive background and faradaic currents by linear fitting, and maximization of the electronic contact area through electrolyte–carbon composites. When these conditions are met, the experimentally determined oxidative stability of hydridoborates is found to be lower than previously reported, but in good agreement with values predicted by first-principle density functional theory calculations combined with grand-potential phase diagram calculations.[58] These findings underscore the importance of carefully selected measurement conditions and illustrate how inappropriate experimental configurations can lead to systematic overestimation of oxidative stability in solid electrolytes.

Even with these refinements, *closo*- and *closo*-carbahydridoborate electrolytes remain among the most oxidation-resistant solid electrolytes known, with experimentally validated oxidative stability limits exceeding 4 V *versus* Li^+/Li for $LiCB_{11}H_{12}$.[29] This remarkable stability is commonly attributed to the highly delocalized charge distribution and aromatic character of the polyhedral boron cluster anions, which render them intrinsically resistant to oxidative decomposition at high potentials. Combined theoretical and experimental studies have shown that electrochemical oxidation of hydridoborates does not proceed *via* abrupt breakdown but instead follows a chemically meaningful cascade of cluster growth reactions. In particular, solid-state oxidation of $LiBH_4$ above ~2.0 V *versus* Li^+/Li leads to the formation of $Li_2B_{12}H_{12}$, followed at higher potentials of ~3.8 V *versus* Li^+/Li by successive oxidation to larger, hydrogen-interconnected (polymerized) *closo*-clusters maintaining the B_{12} units. Grand-canonical phase diagram calculations, including noncrystalline decomposition products, reveal that these polymerized clusters are thermodynamically stable at progressively higher electrochemical potentials, in agreement with experimental observations.[63]

Although these oxidation products are thermodynamically available, their formation can be kinetically hindered under solid-state conditions, effectively extending the apparent electrochemical stability window observed in all-solid-state cells.[58] At high degrees of oxidation, the resulting products are typically neither redox-active nor ionically conductive, as the rotational dynamics are sterically constrained, particularly for larger clusters. These chain-like species interconnected by bridging hydrogen atoms may contribute to the development of a resistive interphase at the cathode–electrolyte interface.[58] Consistent with this picture, cycling beyond the stability window results in increasing cell impedance and ultimately cell failure.[36] Nevertheless, the overarching trend that progressively larger boron–hydrogen clusters formed through oxidation are stabilized at higher electrochemical potentials remains robust across hydridoborate chemistries.

Notably, the transformation from $LiBH_4$ to $Li_2B_{12}H_{12}$ proceeds *via* the transient formation of a highly conductive mixed-anion phase containing both $[BH_4]^-$ and $[B_{12}H_{12}]^{2-}$ species, highlighting the possibility of *in situ* generation of fast-ion-conducting mixed-anion hydridoborates directly within all-solid-state cells.[63] Based on analogous observations from thermal decomposition studies involving other cations, such as Na^+ and Ca^{2+}, similar oxidation cascades involving cluster growth and eventual formation of amorphous boron are anticipated for sodium-based and other divalent-cation-based systems, including $NaBH_4$, $Na_2B_{12}H_{12}$, and $Ca(BH_4)_2$. This suggests that the fundamental oxidation chemistry of hydridoborates is broadly transferable across different charge carriers, with important implications for their electrochemical stability and interfacial behavior.

An equally critical requirement for integrating solid electrolytes into high-energy-density all-solid-state batteries is their stability at low potential, particularly at the interface with lithium and sodium metal. Instabilities at this interface can trigger parasitic reactions, impedance growth, and ultimately reduce cycle life and safety. Understanding the reductive behavior of hydridoborates is therefore essential not only for lithium and sodium metal anodes, but also for alternative low-potential anode materials such as lithiated silicon and sodiated tin, which operate at similarly low electrochemical potentials.

Previous studies on $Li_2B_{12}H_{12}$ and mixed-anion hydridoborates such as $Li_{10}(CB_9H_{10})_7$ $(CB_{11}H_{12})_3$ evaluated reductive stability using stripping/plating experiments in symmetric Li|electrolyte|Li cells. In these experiments, stability was inferred from stable overpotential of lithium stripping/plating. However, the formation of thin layers of reduced electrolyte may not lead to noticeable changes in the overpotential of stripping/plating experiments, which is additionally influenced by morphological changes of the electrodes upon stripping/plating. Furthermore, cycling voltammetry was performed, inferring apparent stability from reversible plating/stripping currents near 0 V *vs.* Li^+/Li.[24,64] However, such measurements cannot distinguish true thermodynamic stability from kinetically hindered decomposition. Similar to the oxidative composition, small reduction currents are easily overlooked at scan rates of 0.5 mV s^{-1}. Indeed, for $Li_2B_{12}H_{12}$ the experimentally inferred stability contradicts theoretical predictions of spontaneous decomposition to LiH and LiB upon contact with lithium metal.

This discrepancy is now understood to arise from slow interfacial decomposition kinetics,[32] masking the onset of electrolyte reduction and giving rise to falsely ''stable'' voltammetric signatures. Detecting reduction currents is further complicated by the intrinsically low current densities associated with electrolyte decomposition, particularly when using planar electrodes with small effective contact areas.

Slow scan rates and/or elevated temperatures enhance the detectability of such weak reduction processes. For example, reduction features in $Li_2B_{12}H_{12}$ become visible above 0 V *vs.* Li^+/Li when voltammetry is performed at 75 °C and 0.5 mV s^{-1}.[65] A recent study combining impedance spectroscopy, coulometric titration time analysis, and slow-scan voltammetry at 60 °C shows consistently that $Li_3(CB_{11}H_{12})_2(CB_9H_{10})$ is not thermodynamically stable against lithium metal, fully in line with density functional theory (DFT) predictions. Theoretical calculations further indicate that structurally related *closo*-hydridoborates (*e.g.*, $Li_2B_{10}H_{10}$ and

$Li_2B_{12}H_{12}$) are also not thermodynamically stable down to 0 V *vs.* Li^+/Li.[32]

Despite this thermodynamic driving force for reduction, hydridoborates exhibit remarkably slow decomposition kinetics at room temperature. This behavior arises from the formation of a passivating solid electrolyte interphase, which leads to transport-limited decomposition. As shown in ref. 32, the decomposition is at least 5 times slower at 25 °C compared to 60 °C. While the thermodynamic stability window itself is not strongly temperature dependent, operation outside the thermodynamic stability window is possible at 25 °C with negligible impedance growth due to transport-limited decomposition, which we refer to as ''kinetic stability''. At high temperatures, the transport-limited reduction accelerates, and thus the thermodynamic instability becomes apparent through impedance growth. This temperature dependence explains earlier reports of apparent electrochemical stability at room temperature and suggests that hydridoborate electrolytes may still be compatible with low-potential anodes such as lithium metal or silicon at moderate temperatures.

Taken together, these insights establish a nuanced but encouraging picture: while hydridoborates are kinetically robust at low potential, the integration of lithium metal anodes still demands careful interface engineering to control inhomogeneous stripping and plating. In the following section, we examine how these considerations translate into the performance and design of solid-state batteries incorporating hydridoborate solid electrolytes.

4. Integration into solid-state batteries

4.1. Compatibility with high-voltage cathodes

The high ionic conductivity and broad electrochemical stability windows of *closo-* and *closo*-carba-hydridoborates provide a solid foundation for their integration into all-solid-state batteries. Beyond these essential properties, hydridoborate electrolytes offer several additional advantages. Their high thermal stability and tolerance to ambient conditions simplify processing, as any absorbed moisture can be removed by vacuum drying.[15,24,66] They are also significantly lighter (crystallographic density 1.05 g cm^{-3} for $Li_3(CB_{11}H_{12})_2(CB_9H_{10})$) than sulfide (*e.g.*, Li_6PS_5Cl, 1.86 g cm^{-3}),[67] halide (*e.g.*, $Li_3In_{0.6}Sc_{0.3}Cl_4$, 2.49 g cm^{-3}),[8] and oxide electrolytes (*e.g.*, LLZO, 5.12 g cm^{-3}),[68] offering the prospect of higher specific energy. We illustrate the effect of electrolyte density on cell-level specific energy with a hypothetical calculation in Fig. 6a, neglecting any kinetic and mass transport limitations, and assuming very thin separators (20 μm). The low density of hydridoborates means that cells with hydridoborate solid electrolytes in this idealized case could reach a target specific energy of 400 Wh kg^{-1} at an areal capacity of 3 mAh cm^{-2}, whereas cells based on sulfide and halide solid electrolyte would require more than 4 mAh cm^{-2}. Cells with LLZO solid electrolyte would only reach 400 Wh kg^{-1} at ultra-high mass loadings of >8 mAh cm^{-2}.

Vice versa, we can also calculate the permissible separator thickness for a fixed areal loading of 6 mAh cm^{-2} (Fig. 6b). For this hypothetical cell setup, oxide electrolytes such as LLZO require separator thicknesses below 10 μm, halides allow 35 μm, and sulfides allow 55 μm. In contrast, hydridoborates can tolerate separator thicknesses of 110 μm while maintaining a specific energy of 400 Wh kg^{-1}. This simple scaling analysis highlights that low electrolyte density directly relaxes the stringent thickness constraints that currently limit oxide- and sulfide-based solid-state batteries. This is especially relevant for applications where specific energy [Wh kg^{-1}] is more important than energy density [Wh L^{-1}], such as *e.g.*, drones and electric aviation.

A key benefit of hydridoborates is their mechanical deformability, comparable to sulfides,[70–72] which facilitates intimate solid–solid contact within composite electrodes and has

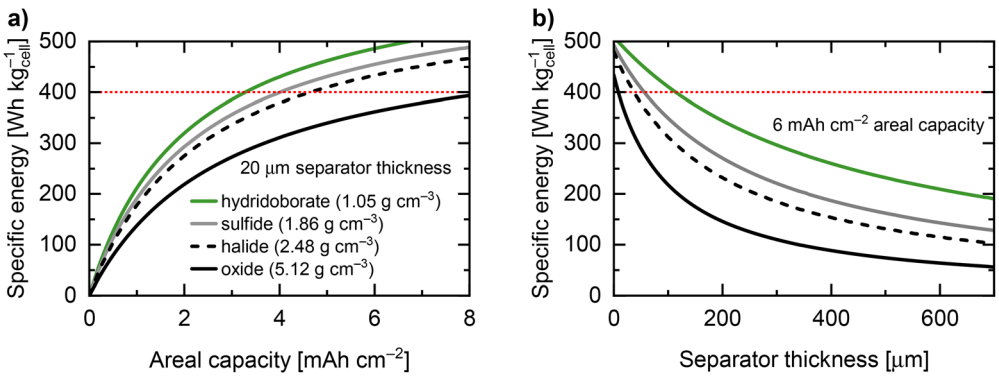

Fig. 6 Hypothetical cell-level specific energy for lithium metal cells as a function of areal capacity (a) and solid electrolyte thickness (b). The data is calculated based on the approach reported by Kravchyk *et al.*[69] with an NMC cathode at 190 mAh g^{-1}, a very low volume fraction of 20 vol% solid electrolyte in the cathode composite, and the remaining 80 vol% consisting of 95 wt% of cathode active material, 3 wt% of carbon black, and 2 wt% of PVDF binder. Any kinetic and mass transport limitations are neglected. The model considers a cell of 20 double-coated cathode layers on aluminum, 19 double-side anode layers on copper, 2 single anode layers, 40 solid electrolyte layers and 2 plastic packaging layers. The lithium metal anode has 20% of the areal capacity of the cathode when the cell is discharged, *i.e.* at 6 mAh cm^{-2} cathode capacity, the lithium metal layer is 5.8 μm thin in the discharged state.

already enabled stable cycling in 4 V class lithium and sodium all-solid-state batteries. For example, cold-pressing dry powders of $LiNi_{0.8}Mn_{0.1}Co_{0.1}O_2$ (NMC811) with $Li_3(CB_{11}H_{12})_2(CB_9H_{10})$ as the solid electrolyte yields composite cathodes with good interfacial contact and stable cycling performance.[29]

A further asset is the solubility of hydridoborates in isopropanol. In the case of $Na_4(B_{12}H_{12})(B_{10}H_{10})$, this solubility is complemented by its ability to recrystallize directly into the highly conductive phase, enabling solution-based processing routes.[44,73] These include solution impregnation of active material particles and infiltration of porous sheet electrodes, see Fig. 7;[73] methods that are compatible with roll-to-roll electrode fabrication as long as the active material is compatible to the solvent. Initially demonstrated for $Na_4(B_{12}H_{12})(B_{10}H_{10})$, solution processing has since been extended to $Na_4(CB_{11}H_{12})_2(B_{12}H_{12})$, for example in combination with $Na_3(VOPO_4)_2F$ as cathode active material.[36]

Beyond these processing advantages, hydridoborates show remarkable robustness when paired with high-voltage cathodes. In Na-based systems, composite cathodes using $Na_3(VOPO_4)_2F$ can be cycled above 4 V *vs.* Na^+/Na with high coulombic efficiency and stable capacities. Stepwise extension of the upper cutoff voltage reveals that even when exceeding the intrinsic thermodynamic stability of $[B_{12}H_{12}]^{2-}$, the less stable anion in the mixed $Na_4(CB_{11}H_{12})_2(B_{12}H_{12})$ electrolyte, the cathode–electrolyte interface remains functional. Electrochemical signatures indicate that oxidative decomposition products of $[B_{12}H_{12}]^{2-}$ are redox-inactive and form a passivating layer at the interface. This self-passivation mechanism stabilizes the interphase and renders protective coatings applied to the cathode materials unnecessary, allowing a 4 V-class sodium all-solid-state battery with a sodium metal anode and a $Na_3(VOPO_4)_2F$ cathode to operate reliably.[36] Long-term cycling stability was demonstrated with 76% capacity retention after 800 cycles (Fig. 8a).

In lithium-based systems, where cathode potentials extend well beyond 4 V and interfacial reactivity differs, a complementary strategy has proven effective. Integration with high-nickel $LiNi_{0.8}Mn_{0.1}Co_{0.1}O_2$ (NMC811) cathodes benefits from targeted interface engineering, for example through bulk titanium doping combined with a thin TiO_2 coating. This coating is sufficient to prevent detrimental electrolyte oxidation, enabling highly reversible cycling. Cells with In/InLi and graphite anodes paired with NMC811 as cathode active material and a hydridoborate solid electrolyte achieve exceptional stability, retaining ~97–98% of the cathode capacity after 100 cycles at room temperature. With specific energies around 460 Wh kg^{-1} per cathode composite, these hydridoborate-based cells reach performance levels comparable to the best solid-state batteries reported to date.[29] Long-term cycling stability was demonstrated with 70% capacity retention after 1000 cycles (Fig. 8b).

Overall, the combination of mechanical compliance, solution processability, and robust interfacial behavior, supported by self-passivating decomposition layers (Na systems) and/or minimal artificial coatings (Li systems), positions *closo*- and *closo*-carba-hydridoborates as highly promising solid electrolytes for integrating high-voltage cathodes in next-generation solid-state batteries.

4.2. Compatibility with metal and alloy-type anodes

While hydridoborate solid electrolytes show excellent compatibility with high-voltage cathodes, their integration with high-capacity negative electrodes at industry-relevant areal capacities is considerably more challenging. Alkali metal anodes are inherently challenging to use, independent of the solid electrolyte, due to inhomogeneous stripping and plating, leading to void formation, interface roughening, metal dendrite growth, and ultimately cell failure.[74] These phenomena limit the practically accessible areal capacities and current densities. Thereby the mechanical properties of the alkali metal have a strong influence on the anode/electrolyte interface. Experimental comparisons between garnet-type $Li_7La_3Zr_2O_{12}$ and Na-β″-alumina further support this view: Na systems exhibit significantly higher critical current densities than Li systems, a difference attributed to the distinct mechanical and diffusive properties of the two alkali metals, including the lower melting point and enhanced deformability of sodium.[75] Thus, Li metal imposes far stricter requirements on the solid electrolyte to suppress dendrites than its Na metal counterpart.

Alloy-type or intercalation anodes, including In–Li, Na–Sn, carbonaceous materials, or silicon, circumvent many of the intrinsic instabilities of Li metal because they do not rely on homogeneous metal stripping and plating. Their main drawback is the added weight and volume of the host matrix, which reduces the cell-level specific energy and energy density. Among these alternatives, silicon stands out with a gravimetric capacity close to that of Li metal (up to 3600 mAh g^{-1} at $Li_{3.75}Si$) combined with a higher average lithiation potential (≈0.1 V *vs.* Li^+/Li), effectively mitigating the risk of dendrite formation. However, silicon exhibits large volume changes that induce particle fracture and repeated solid electrolyte interphase

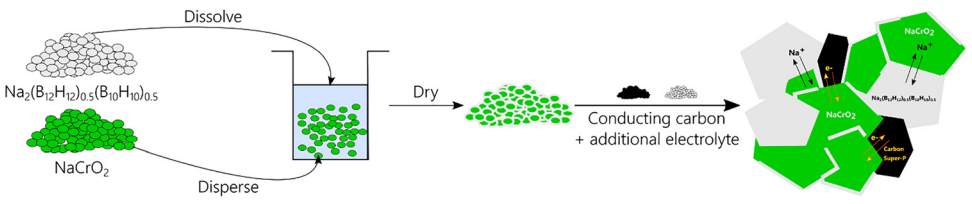

Fig. 7 Solution processing of $Na_4(B_{12}H_{12})(B_{10}H_{10})$.

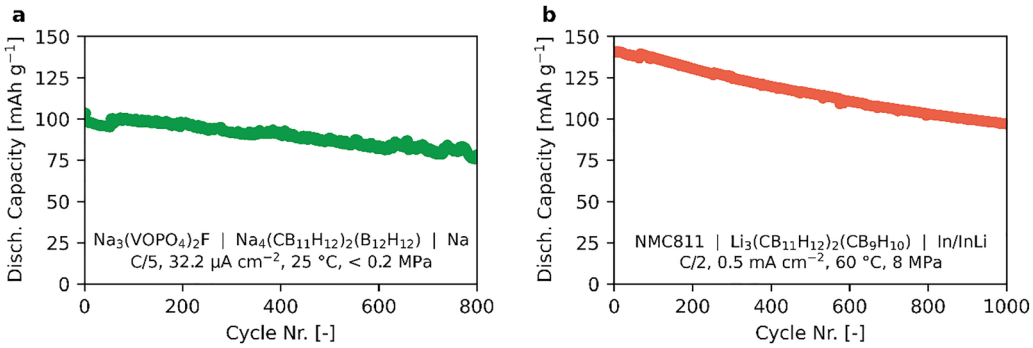

Fig. 8 Long-term cycling stability of (a) Na | $Na_4(CB_{11}H_{12})_2(B_{12}H_{12})$ | $Na_3(VOPO_4)_2F$ all-solid-state batteries and of (b) In/InLi | $Li_3(CB_{11}H_{12})_2(CB_9H_{10})$ | NMC811 solid-state batteries. Figures are modified from ref. 36 and 29 with permission from the Royal Society of Chemistry[36] and the American Chemical Society[29] copyright 2020 and 2024, respectively.

reformation in conventional liquid electrolytes, resulting in continuous electrolyte consumption and poor cycling stability.[76]

Solid-state electrolytes offer a potential route to stabilize silicon electrodes, but sulfide electrolytes such as Li_6PS_5Cl are reduced at low potentials, forming Li_2S, Li_3P, and LiCl.[77] This chemical instability leads to rapid interfacial degradation in Si–sulfide composite electrodes, manifested in severe impedance growth ($\sim$10 Ω cm^2 h$^{-0.5}$), low initial coulombic efficiencies ($<$60%), and fast capacity fading ($\leq$10–20% retention after 100 cycles). Carbon additives and nanosized Si, beneficial for achieving high capacity and good rate performance, further accelerate electrolyte decomposition, rendering sulfide-based silicon composites unsuited for realistic cycling conditions.[78]

By contrast, hydridoborate electrolytes exhibit far superior compatibility with silicon. Recent work demonstrates that the carba-hydridoborate electrolyte $Li_3(CB_{11}H_{12})_2(CB_9H_{10})$ can be integrated into silicon composite anodes with negligible parasitic reactivity and dramatically reduced interfacial degradation (impedance growth $\sim$0.3 Ω cm^2 h$^{-0.5}$ and initial coulombic efficiency of up to 96%).[79] Even though silicon electrodes operate outside the thermodynamic stability window of lithium hydridoborates,[32] the transport-limited reduction kinetics are sufficiently slow such that electrolyte reduction is essentially not observable under typical cycling conditions.[79] This property is referred to as ''kinetic stability''. The kinetic stability of hydridoborates enables the use of nanosized silicon particles and carbon additives without excessive electrolyte reduction. These silicon–hydridoborate composites operate reliably at moderate stack pressures ($\sim$8 MPa) and achieve industry-relevant areal capacities ($\sim$3 mAh cm^{-2}) at room temperature. Combined with NMC811 cathodes, zero-lithium-excess hydridoborate solid-state batteries were demonstrated, highlighting the promise of silicon as a practical negative electrode in this family of materials. Stack pressures in the range of a few MPa are commonly used across all classes of solid electrolytes to improve densification and interfacial contact, and hydridoborates are no exception. These pressures have only a limited effect on intrinsic ionic conductivity.

Going forward, progress in hydridoborate-based solid-state batteries will depend on developing thin, mechanically robust separator layers, improving lithium transport through the NMC811 composite cathode, and refining electrode architectures that accommodate volume change while preserving intimate solid–solid contact. Together, these advances may unlock anode-free or low-Li-excess hydridoborate solid-state batteries that circumvent the challenges of Li metal while retaining high cell-level specific energy.

5. Outlook and perspectives

Future progress of hydridoborate electrolytes hinges on developing cost-effective and scalable synthetic routes. Transitioning from high-cost carborane precursors to readily available borohydride sources such as $NaBH_4$ would substantially improve sustainability and facilitate broader adoption. Mechanochemical synthesis and solvent-free metathesis are particularly promising in this regard, offering environmentally benign pathways that eliminate the need for hazardous solvents and are compatible with large-scale production.

Processing remains another central challenge and opportunity. The intrinsic mechanical softness of hydridoborates enables cold pressing and other low-temperature consolidation methods that avoid the use of solvents. Their deformability offers a practical pathway toward dry processing of full cells. Meanwhile more work is needed to bring stack-pressure requirements down to application-relevant levels of $\sim$0.1 MPa without sacrificing capacity retention. Optimizing the mechanical properties of hydridoborate electrolytes while maintaining high ionic conductivity will be essential for reliable cell engineering. Hybrid electrolytes that combine hydridoborates with polymers or oxides may provide an additional route to balance flexibility, transport, and interfacial stability, aligning well with ongoing efforts to design composite electrolytes with tailored mechanical and electrochemical characteristics.

The structural versatility of *closo*- and *closo*-carba-hydridoborate frameworks extends beyond Li^+ conductors. Sodium analogues already exhibit promising ion transport, and first-principles studies further suggest that multivalent cations such as Ca^{2+} may also be accommodated within these

anion frameworks. In the case of $CaB_{12}H_{12}$, computational work predicts percolating Ca^{2+} migration pathways with moderate activation barriers, although experimental demonstrations as solid electrolytes or in solid-state cells are still pending.[80] Recent work indicates that $Ca(CB_{11}H_{12})_2$ can achieve significant solid-state Ca^{2+} conductivity and reversible Ca^{2+} migration in symmetric cells, highlighting the potential of carba-hydridoborates for multivalent solid electrolytes.[81] For $MgB_{12}H_{12}$, synthesis and structural characterization have been reported, but its role as a solid ionic conductor has not yet been established.[39] Thus, while the underlying structural motifs appear broadly compatible with monovalent and potentially multivalent transport, practical solid-state electrolyte realizations beyond Li^+ and Na^+ are still at an early stage.

Chemical and morphological interfacial stability will remain a decisive factor for practical cell performance. Hydridoborate electrolytes show excellent compatibility with high-voltage cathodes, but interfaces with alkali metal anodes remain inherently challenging due to inhomogeneous stripping and plating, void formation, and metal dendrite growth; issues intrinsic to metal anodes themselves, independent of the electrolyte. Engineering kinetically stable interphases or artificial buffer layers may offer viable routes to circumvent these limitations. Ultimately, zero-lithium-excess or anode-free configurations are desirable, maximizing specific energy and energy density while reducing safety risks.

A deeper understanding of the structure–transport–stability relationships will be crucial. *Operando* characterization techniques capable of probing buried interfaces, mechanical evolution, and ion dynamics across multiple length scales remain underdeveloped for hydridoborate-based systems. Advances in μXRD, neutron scattering, tomography, and spectro-electrochemical methods will be essential to resolve the complex changes occurring during cycling and to inform materials design.

The evolution from simple borohydrides to complex *closo*- and *closo*-carba-hydridoborate electrolytes represents a major advance in solid-state ionics. Their exceptional ionic conductivity, broad electrochemical stability, mechanical compliance, and chemical benignity position them among the most promising candidates for next-generation solid-state batteries. Continued progress in cost-effective synthesis, interfacial engineering, *operando* diagnostics, and scalable processing will ultimately determine whether these materials can transition from laboratory demonstrations to robust, commercially relevant technologies.

Author contributions

A. R. led the study and wrote the manuscript. H. B. supported the development of the research context, contributed ideas and manuscript feedback, carried out the cell-level specific energy calculations and assisted with the figures. C. B. provided project supervision and critically reviewed and approved the final manuscript.

Conflicts of interest

There are no conflicts to declare.

Data availability

No new data were generated during this review study. All analyzed data originate from previously published literature sources, which are properly cited throughout the manuscript and listed in the reference section.

References

1 J. Janek and W. G. Zeier, *Nat. Energy*, 2016, **1**, 16141.
2 N. Zhao, W. Khokhar, Z. Bi, C. Shi, X. Guo, L.-Z. Fan and C.-W. Nan, *Joule*, 2019, **3**, 1190–1199.
3 K. S. Ngai, S. Ramesh, K. Ramesh and J. C. Juan, *Ionics*, 2016, **22**, 1259–1279.
4 X. Zhao, C. Wang, H. Liu, Y. Liang and L.-Z. Fan, *Batteries Supercaps*, 2023, **6**, e202200502.
5 Y. Zhao, L. Wang, Y. Zhou, Z. Liang, N. Tavajohi, B. Li and T. Li, *Adv. Sci.*, 2021, **8**, 2003675.
6 S. P. Culver, R. Koerver, W. G. Zeier and J. Janek, *Adv. Energy Mater.*, 2019, **9**, 1900626.
7 J. Liang, X. Li, C. Wang, J. T. Kim, R. Yang, J. Wang and X. Sun, *Energy Mater. Adv.*, 2023, **4**, 0021.
8 L. Zhou, T.-T. Zuo, C. Y. Kwok, S. Y. Kim, A. Assoud, Q. Zhang, J. Janek and L. F. Nazar, *Nat. Energy*, 2022, **7**, 83–93.
9 J. Cao, J. Meng, H. Shen, X. Ye, H. Liu, C. Guo, J. Li, G. Zhang, W. Bao and F. Yu, *J. Power Sources*, 2025, **654**, 237870.
10 X. Gao, Y.-N. Zhou, D. Han, J. Zhou, D. Zhou, W. Tang and J. B. Goodenough, *Joule*, 2020, **4**, 1864–1879.
11 Y. Lu, C.-Z. Zhao, H. Yuan, X.-B. Cheng, J.-Q. Huang and Q. Zhang, *Adv. Funct. Mater.*, 2021, **31**, 2009925.
12 L. Duchêne, A. Remhof, H. Hagemann and C. Battaglia, *Energy Storage Mater.*, 2020, **25**, 782–794.
13 M. Matsuo, Y. Nakamori, S.-I. Orimo, H. Maekawa and H. Takamura, *Appl. Phys. Lett.*, 2007, **91**, 224103.
14 H. Maekawa, M. Matsuo, H. Takamura, M. Ando, Y. Noda, T. Karahashi and S.-I. Orimo, *J. Am. Chem. Soc.*, 2009, **131**, 894–895.
15 L. Duchêne, R. S. Kühnel, D. Rentsch, A. Remhof, H. Hagemann and C. Battaglia, *Chem. Commun.*, 2017, **53**, 4195–4198.
16 Y. Yan, R. S. Kühnel, A. Remhof, L. Duchêne, E. C. Reyes, D. Rentsch, Z. Lodziana and C. Battaglia, *Adv. Energy Mater.*, 2017, **7**, 1700294.
17 W. Zeng, Q. Gao and Y. Tang, *ACS Appl. Energy Mater.*, 2025, **8**, 16750–16758.
18 P. Dansirima, L. G. Kristensen, J. B. Grinderslev, J. Skibsted, R. Utke and T. R. Jensen, *Commun. Mater.*, 2024, **5**, 160.
19 V. Gulino, L. Barberis, P. Ngene, M. Baricco and P. E. de Jongh, *ACS Appl. Energy Mater.*, 2020, **3**, 4941–4948.
20 S. Kim, N. Toyama, H. Oguchi, T. Sato, S. Takagi, T. Ikeshoji and S.-I. Orimo, *Chem. Mater.*, 2018, **30**, 386–391.
21 A. Garcia, G. Mueller, R. Černý, D. Rentsch, R. Asakura, C. Battaglia and A. Remhof, *J. Mater. Chem. A*, 2023, **11**, 18996–19003.
22 M. Jorgensen, P. T. Shea, A. W. Tomich, J. B. Varley, M. Bercx, S. Lovera, R. Černý, W. Zhou, T. J. Udovic, V. Lavallo, T. R. Jensen, B. C. Wood and V. Stavila, *Chem. Mater.*, 2020, **32**, 1475–1487.
23 K. E. Kweon, J. B. Varley, P. Shea, N. Adelstein, P. Mehta, T. W. Heo, T. J. Udovic, V. Stavila and B. C. Wood, *Chem. Mater.*, 2017, **29**, 9142–9153.
24 S. Kim, H. Oguchi, N. Toyama, T. Sato, S. Takagi, T. Otomo, D. Arunkumar, N. Kuwata, J. Kawamura and S. Orimo, *Nat. Commun.*, 2019, **10**, 1081.
25 S. Kim, K. Kisu, S. Takagi, H. Oguchi and S.-I. Orimo, *ACS Appl. Energy Mater.*, 2020, **3**, 4831–4839.
26 W. S. Tang, A. Unemoto, W. Zhou, V. Stavila, M. Matsuo, H. Wu, S. Orimo and T. J. Udovic, *Energy Environ. Sci.*, 2015, **8**, 3637–3645.

27 W. S. Tang, K. Yoshida, A. V. Soloninin, R. V. Skoryunov, O. A. Babanova, A. V. Skripov, M. Dimitrievska, V. Stavila, S.-I. Orimo and T. J. Udovic, *ACS Energy Lett.*, 2016, **1**, 659–664.
28 L. Duchêne, S. Lunghammer, T. Burankova, W.-C. Liao, J. P. Embs, C. Copéret, H. M. R. Wilkening, A. Remhof, H. Hagemann and C. Battaglia, *Chem. Mater.*, 2019, **31**, 3449–3460.
29 H. Braun, R. Asakura, A. Remhof and C. Battaglia, *ACS Energy Lett.*, 2024, **9**, 707–714.
30 J. A. S. Oh, Z. Yu, C.-J. Huang, P. Ridley, A. Liu, T. Zhang, B. J. Hwang, K. J. Griffith, S. P. Ong and Y. S. Meng, *Joule*, 2025, **9**, 102130.
31 M. Brighi, F. Murgia, Z. Łodziana, P. Schouwink, A. Wołczyk and R. Cerny, *J. Power Sources*, 2018, **404**, 7–12.
32 H. Braun, Z. Łodziana, C. Battaglia and A. Remhof, *J. Mater. Sci.: Mater. Energy*, 2026, **2**, 2.
33 J. L. Hempel, S. Thapa, K. Kim, K. E. Kweon, B. C. Wood, Y. V. Sevryugina, R. Mohtadi, O. Tutusaus and Y.-T. Cheng, *J. Power Sources*, 2025, **641**, 236800.
34 R. Asakura, A. Remhof and C. Battaglia, in *Solid State Batteries Volume 1: Emerging Materials and Applications*, American Chemical Society, 2022, vol. 1413, ch. 14, pp. 353–393.
35 B. R. S. Hansen, M. Paskevicius, H.-W. Li, E. Akiba and T. R. Jensen, *Coord. Chem. Rev.*, 2016, **323**, 60–70.
36 R. Asakura, D. Reber, L. Duchêne, S. Payandeh, A. Remhof, H. Hagemann and C. Battaglia, *Energy Environ. Sci.*, 2020, **13**, 5048–5058.
37 Y. Yan, A. Remhof, S.-J. Hwang, H.-W. Li, P. Mauron, S.-I. Orimo and A. Züttel, *Phys. Chem. Chem. Phys.*, 2012, **14**, 6514–6519.
38 H. C. Miller, N. E. Miller and E. L. Muetterties, *J. Am. Chem. Soc.*, 1963, **85**, 3885–3886.
39 A. Remhof, Y. Yan, D. Rentsch, A. Borgschulte, C. M. Jensen and A. Züttel, *J. Mater. Chem. A*, 2014, **2**, 7244–7249.
40 V. Geis, K. Guttsche, C. Knapp, H. Scherer and R. Uzun, *Dalton Trans.*, 2009, 2687–2694.
41 C. Housecroft and E. Constable, *Chemistry: An introduction to organic, inorganic and physical chemistry*, Pearson Education, 4th edn, 2010.
42 E. L. Muetterties, J. H. Balthis, Y. T. Chia, W. H. Knoth and H. C. Miller, *Inorg. Chem.*, 1964, **3**, 444–451.
43 L. He, H.-W. Li, S.-J. Hwang and E. Akiba, *J. Phys. Chem. C*, 2014, **118**, 6084–6089.
44 A. Gigante, L. Duchene, R. Moury, M. Pupier, A. Remhof and H. Hagemann, *ChemSusChem*, 2019, **12**, 4832–4837.
45 W. H. Knoth Jr., *Inorg. Chem.*, 1971, **10**, 598–605.
46 J. Plešek, T. Jelínek, E. Drdáková, S. Heřmánek and B. Štíbr, *Collect. Czech. Chem. Commun.*, 1984, **49**, 1559–1562.
47 A. Franken, B. T. King, J. Rudolph, P. Rao, B. C. Noll and J. Michl, *Collect. Czech. Chem. Commun.*, 2001, **66**, 1238–1249.
48 A. Berger, C. E. Buckley and M. Paskevicius, *Inorg. Chem.*, 2021, **60**, 14744–14751.
49 J. Kulenkampff, C. Armbruster, J. Drolshagen, C. Regnat, T. Wienold, L. Spari, J. Fix, T. Sterbak, H. Scherer and I. Krossing, *Chem.: Methods*, 2024, **4**, e202400011.
50 J. Timmermans, *J. Phys. Chem. Solids*, 1961, **18**, 1–8.
51 R. Černý, M. Brighi and F. Murgia, *Chemistry*, 2020, **2**, 805–826.
52 L. Pauling, *J. Am. Chem. Soc.*, 1929, **51**, 1010–1026.
53 N. Verdal, J.-H. Her, V. Stavila, A. V. Soloninin, O. A. Babanova, A. V. Skripov, T. J. Udovic and J. J. Rush, *J. Solid State Chem.*, 2014, **212**, 81–91.
54 A. V. Skripov, A. V. Soloninin, O. A. Babanova and R. V. Skoryunov, *Molecules*, 2020, **25**, 2940.
55 N. Verdal, T. J. Udovic, V. Stavila, W. S. Tang, J. J. Rush and A. V. Skripov, *J. Phys. Chem. C*, 2014, **118**, 17483–17489.
56 F. Han, T. Gao, Y. Zhu, K. J. Gaskell and C. Wang, *Adv. Mater.*, 2015, **27**, 3473–3483.
57 K. H. Park, Q. Bai, D. H. Kim, D. Y. Oh, Y. Zhu, Y. Mo and Y. S. Jung, *Adv. Energy Mater.*, 2018, **8**, 1800035.
58 R. Asakura, L. Duchêne, R. S. Kühnel, A. Remhof, H. Hagemann and C. Battaglia, *ACS Appl. Energy Mater.*, 2019, **2**, 6924–6930.
59 F. Han, Y. Zhu, X. He, Y. Mo and C. Wang, *Adv. Energy Mater.*, 2016, **6**, 1501590.
60 F. Han, T. Gao, Y. Zhu, K. J. Gaskell and C. Wang, *Adv. Energy Mater.*, 2016, **6**, 1501590.
61 Y. Sadikin, M. Brighi, P. Schouwink and R. Černý, *Adv. Energy Mater.*, 2015, **5**, 1501016.
62 M. Matsuo and S.-I. Orimo, *Adv. Energy Mater.*, 2011, **1**, 161–172.
63 R. Asakura, Z. Łodziana, R. Grissa, D. Rentsch, C. Battaglia and A. Remhof, *ACS Appl. Energy Mater.*, 2025, **8**, 9637–9645.
64 A. Unemoto, K. Yoshida, T. Ikeshoji and S.-I. Orimo, *Mater. Trans.*, 2016, **57**, 1639–1644.
65 X. Shi, Y. Pang, B. Wang, H. Sun, X. Wang, Y. Li, J. Yang, H. W. Li and S. Zheng, *Mater. Today Nano*, 2020, **10**, 100079.
66 M. P. Pitt, M. Paskevicius, D. H. Brown, D. A. Sheppard and C. E. Buckley, *J. Am. Chem. Soc.*, 2013, **135**, 6930–6941.
67 G. F. Dewald, S. Ohno, M. A. Kraft, R. Koerver, P. Till, N. M. Vargas-Barbosa, J. Janek and W. G. Zeier, *Chem. Mater.*, 2019, **31**, 8328–8337.
68 A. Logéat, T. Köhler, U. Eisele, B. Stiaszny, A. Harzer, M. Tovar, A. Senyshyn, H. Ehrenberg and B. Kozinsky, *Solid State Ionics*, 2012, **206**, 33–38.
69 K. V. Kravchyk, F. Okur and M. V. Kovalenko, *ACS Energy Lett.*, 2021, **6**, 2202–2207.
70 Z. Lu and F. Ciucci, *Chem. Mater.*, 2017, **29**, 9308–9319.
71 R. Moury, Z. Lodziana, A. Remhof, L. Duchêne, E. Roedern, A. Gigante and H. Hagemann, *Acta Crystallogr., Sect. B*, 2019, **75**, 406–413.
72 H. Chen and T. Hong, *J. Electrochem. Soc.*, 2019, **166**, A493.
73 L. Duchêne, D. H. Kim, Y. B. Song, S. Jun, R. Moury, A. Remhof, H. Hagemann, Y. S. Jung and C. Battaglia, *Energy Storage Mater.*, 2020, **26**, 543–549.
74 K. B. Hatzell, X. C. Chen, C. L. Cobb, N. P. Dasgupta, M. B. Dixit, L. E. Marbella, M. T. McDowell, P. P. Mukherjee, A. Verma, V. Viswanathan, A. S. Westover and W. G. Zeier, *ACS Energy Lett.*, 2020, **5**, 922–934.
75 M. C. Bay, M. Wang, R. Grissa, M. V. F. Heinz, J. Sakamoto and C. Battaglia, *Adv. Energy Mater.*, 2020, **10**, 1902899.
76 G. F. I. Toki, M. K. Hossain, W. U. Rehman, R. Z. A. Manj, L. Wang and J. Yang, *Ind. Chem. Mater.*, 2024, **2**, 226–269.
77 D. H. S. Tan, Y.-T. Chen, H. Yang, W. Bao, B. Sreenarayanan, J.-M. Doux, W. Li, B. Lu, S.-Y. Ham, B. Sayahpour, J. Scharf, E. A. Wu, G. Deysher, H. E. Han, H. J. Hah, H. Jeong, J. B. Lee, Z. Chen and Y. S. Meng, *Science*, 2021, **373**, 1494–1499.
78 H. Huo, M. Jiang, Y. Bai, S. Ahmed, K. Volz, H. Hartmann, A. Henss, C. V. Singh, D. Raabe and J. Janek, *Nat. Mater.*, 2024, **23**, 543–551.
79 H. Braun, C. Bürgel, E. Quérel, A. Remhof and C. Battaglia, *EES Batteries*, 2026, **2**, 597–608.
80 J. Koettgen, C. J. Bartel, J.-X. Shen, K. A. Persson and G. Ceder, *Phys. Chem. Chem. Phys.*, 2020, **22**, 27600–27604.
81 T. Shinohara, K. Kisu, S. Takagi and S.-I. Orimo, *Energy Adv.*, 2024, **3**, 2758–2763.